

promoting access to White Rose research papers



Universities of Leeds, Sheffield and York
<http://eprints.whiterose.ac.uk/>

This is an author produced version of a paper published in **Solar Physics**.

White Rose Research Online URL for this paper:

<http://eprints.whiterose.ac.uk/9289>

Published paper

Fedun, V., Erdelyi, R., Shelyag, S. (2009) *Oscillatory response of the 3D solar atmosphere to the leakage of photospheric motion*, Solar Physics, 258 (2), pp.219-241

<http://dx.doi.org/10.1007/s11207-009-9407-9>

MHD waves became directly detected by these satellites (see e.g. Aschwanden, 2004 for an extensive textbook summary or Banerjee *et al.*, 2007 for the latest paper review). It is known that periodic and spatially coherent photospheric motions have a peak in power at around 5 minutes in the photosphere. There is also a range of observations of periodic phenomena reporting the presence of 5-minute periods in the chromosphere and corona (see, in the context of spicules and transition region oscillations e.g. De Pontieu, Tarbell and Erdélyi, 2003; De Pontieu, Erdélyi and De Wijn, 2003; or in the context of sunspots e.g. Marsh, and Walsh, 2006). De Moortel *et al.*, 2002 claims that the periodicity of intensity oscillations observed in the corona can apparently be divided into two distinct categories: periods found in loops above sunspots are of the order of 3 minutes, whereas periods in non-sunspot loops are at about 5 minutes.

It is of great practical interest to investigate the origin of some of these observed oscillations. Are they indeed directly linked to the photospheric 5-minute power peak? Some further examples of correlated 5-minute oscillations in the transition region and corona have been found by Marsh *et al.*, 2003 with the SOHO Coronal Diagnostic Spectrometer and were recently also reported by Finsterle *et al.*, 2008. De Pontieu, Erdélyi and James, 2004 point out that photospherically driven longitudinal velocity signals may propagate through the upper photosphere and into the chromosphere. They directly associate this wave propagation with the formation of solar spicules. The scenario that can contribute to the explanation of not only the presence of 5-minute waves in the corona, but also their relationship to similar oscillations in the chromosphere and transition region, was reported by De Pontieu, Erdélyi and De Moortel, 2005 in the framework of 1D MHD using field-aligned coordinates.

Numerous studies embarked on MHD wave simulations in different magnetic structures embedded in the solar atmosphere. Pioneering numerical investigations of MHD wave propagation in the solar atmosphere were carried out by e.g. Nakagawa, 1981; Shibata, 1983. More recent numerical simulations of wave propagation in a one- and two-dimensional vertically stratified and non-magnetically/magnetically structured solar atmosphere were carried out by Oliver and Ballester, 1995; Ofman and Davila, 1998; Ofman, Nakariakov and Sehgal, 2000; Bogdan *et al.*, 2003; Hasan *et al.*, 2005; Hansteen *et al.*, 2006; Heggland *et al.*, 2007; Erdélyi *et al.*, 2007; Hasan & van Ballegoijen, 2008 and others. A common shortage of these previous examples is the lack of collective coupling from the photosphere into the corona. The real difficulty there is to resolve the role of the thin transition region in a three-dimensional gravitationally stratified atmosphere. The presence of magnetic field or a realistic magnetic structure pushes the numerical studies to the limits of capacity and capability of recent computer powers.

There are a number of models of magneto-atmospheres that can be used to describe the physical phenomena of the wave propagation in structures like coronal plumes, magnetic prominences, large-scale coronal loops, etc. Perhaps the first complication of the problem is to build a numerically stable equilibrium with these different magnetic structures in three-dimensional space. Wu *et al.*, 2001 constructed a three-dimensional, time-dependent, numerical MHD model

for the investigation of global large amplitude waves (Moreton waves) propagating across the solar disk. The interaction between fast magnetosonic waves with solar active regions was investigated by Ofman and Thompson, 2002 using a resistive 3D MHD model with gravity and finite plasma pressure. In the work of Gudiksen and Nordlund, 2002 the 3D MHD code of Nordlund and Galsgaard, 1995 was adopted for the simulation of a typical scaled-down active region, that included a realistic photospheric driver. In their model the magnetic field was derived from SOHO/MDI magnetograms to construct a potential magnetic field in the computational domain. This is a route that is definitely worth to follow. Recently a 3D numerical model from the upper convection zone to the lower corona was constructed by Hansteen, Carlsson and Gudiksen, 2007. Their approach includes a non-grey, non-local thermodynamic equilibrium with radiative transport in the photosphere and chromosphere, optically thin radiative losses as well as magnetic field-aligned heat conduction in the transition region and corona.

In this paper we extend the approach of Erdélyi *et al.*, 2007; Malins & Erdélyi, 2007 to three-dimensional simulations including the transition region and corona with specific attention to MHD waves generated by photospheric motions. We wish to demonstrate how the leakage of a range of photospheric periodic motions may survive their journey through a gravitationally stratified 3D atmosphere. An equilibrium model is constructed based on the VAL IIIC model (Vernazza, Avrett and Loeser, 1981) combined with an extension into the corona (McWhirter, Thonemann and Wilson, 1975). In particular, two types of computational equilibria are considered here: (i) non-magnetic atmosphere, and (ii) an atmosphere embedded in a uniform vertical magnetic field.

2. Numerical model

To solve numerically the full 3D ideal MHD problem of the time dependent evolution of photospheric oscillations in the solar atmosphere the Versatile Advection Code (VAC) by Tóth, 1996 was further developed. VAC itself is aimed to advance a system of hyperbolic equations by a number of different computational schemes in one, two, or three dimensions in a choice of different geometries (Cartesian, cylindrical, or spherical) with uniform or non-uniform grids. For the present purpose the code was especially modified to solve the ideal MHD equations in a three-dimensional Cartesian domain with perturbed three-dimensional scalar and vector quantities. On the details of shock handling, boundary conditions and the implemented numerical scheme see Shelyag, Fedun and Erdélyi, 2008. The governing equations read as:

$$\frac{\partial \rho \mathbf{V}}{\partial t} + \nabla \cdot (\mathbf{V} \rho \mathbf{V} - \mathbf{B} \mathbf{B}) + \nabla p_{tot} = -(\nabla \cdot \mathbf{B}) \mathbf{B} + \rho \mathbf{g}, \quad (1)$$

$$\frac{\partial \rho}{\partial t} + \nabla \cdot (\rho \mathbf{V}) = 0, \quad (2)$$

$$\frac{\partial e}{\partial t} + \nabla \cdot (\mathbf{V} e - \mathbf{B} \mathbf{B} \cdot \mathbf{V} + \mathbf{V} p_{tot}) = -(\nabla \cdot \mathbf{B}) \mathbf{B} \cdot \mathbf{V} + \rho \mathbf{g} \cdot \mathbf{V}, \quad (3)$$

$$\frac{\partial \mathbf{B}}{\partial t} + \nabla \cdot (\mathbf{V}\mathbf{B} - \mathbf{B}\mathbf{V}) = (\nabla \cdot \mathbf{B})\mathbf{V}, \quad (4)$$

$$p = (\gamma - 1)(e - \rho V^2/2 - B^2/2), \quad (5)$$

$$p_{tot} = p + B^2/2, \quad (6)$$

where ρ is the density, $\vec{V} = (V_x, V_y, V_z)$ is the velocity vector, $\vec{B} = (B_x, B_y, B_z)$ is the magnetic field vector, $e = p/(\gamma - 1) + \rho V^2/2 + B^2/2$ is the total energy density per unit volume, p is the kinetic gas pressure, γ is the adiabatic index, $\vec{g} = (0, 0, -g_z)$ is the solar gravitational acceleration vector, and t is time. g_z denotes the constant gravitational acceleration of 274 m/s². The adiabatic gas index γ , assumed to be constant over the computational domain, is equal to 5/3. The magnetic field is rescaled as $\mathbf{B} = \mathbf{B}/\sqrt{\mu}$. The terms that are proportional to $\nabla \cdot \mathbf{B}$ on the RHS are necessary in order to eliminate numerical problems related to the divergence of the magnetic field (see Tóth, 1996 for a comprehensive discussion about the divergence problem).

A fourth-order accurate method involving the two nearest neighbouring points on each side is used for determining the partial spatial derivatives. The equations are stepped forward in time using a fourth-order Runge-Kutta method. In order to decrease the numerical noise, high-order artificial diffusion is added (see Nordlund and Galsgaard, 1995; Shelyag, Fedun and Erdélyi, 2008). More technical details with a number of test cases on the numerical solutions of a gravitationally stratified and magnetised plasma can be found in Shelyag, Fedun and Erdélyi, 2008.

A typical simulation domain is shown in Figure 1. The box is 4 Mm wide in the x and y directions and 8 Mm high in the vertical z direction, and has a resolution of $144 \times 144 \times 512$ grid points, respectively. The upper boundary of the domain is well within the solar corona. We consider this setup and effort as a very important

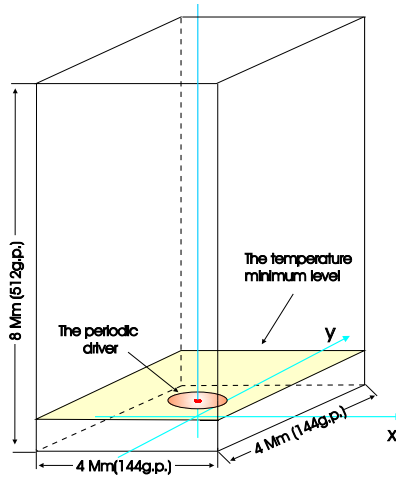


Figure 1. Schematic plot of the on computational configuration. The temperature minimum level (yellow plane) and position of the periodic driver (red enclosed circle in the middle) are highlighted in the plot.

step forward from related similar works (e.g. Bogdan *et al.*, 2003; Hasan & van Ballegoijen, 2008) as here we will be able to capture the role of the transition region. Further, since our boundary conditions are open, we are not bound by the time limit of (magneto)acoustic perturbations reaching the upper boundary. In practice this means we are able to perform simulations well above 100 s of wave propagation time, i.e. we have the chance to capture a few periods of e.g. wave propagation with 5-minute period. The temperature profile in the numerical simulations is based on the VAL IIIIC model atmosphere below the transition region, and the McWhirter, Thonemann and Wilson, 1975 model atmosphere above it. Vertical cuts of the temperature and density structures are shown in Figure 2. Therefore, one can conclude that the equilibrium box consists of three

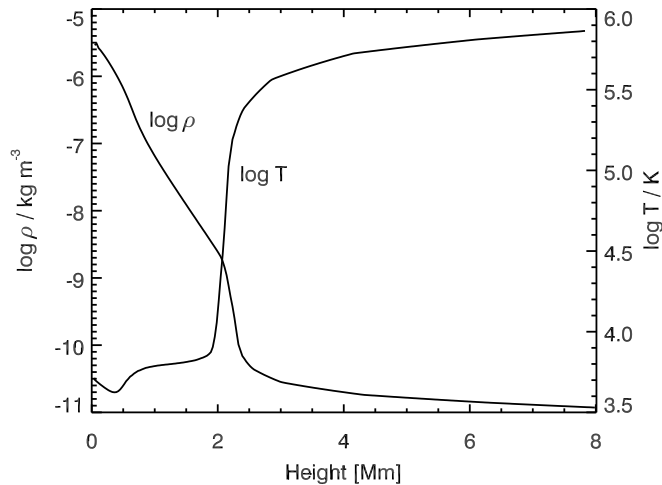


Figure 2. Density and temperature profiles as functions of height z . These profiles are constructed by the combination of the VAL IIIIC model atmosphere below the transition region and by the McWhirter model of solar corona above it.

distinct parts: the lower part of the numerical domain corresponds to the solar photospheric level with the temperature minimum region and the chromosphere approximately at 0.2-2 Mm in height measured from the bottom plate of the domain; the narrow transition region at 2 Mm, and the solar coronal region up to 8 Mm in height. The density and pressure profiles for the non-magnetic atmosphere are constructed from the temperature profile assuming the condition of hydrostatic equilibrium:

$$\frac{dp}{dz} = -\rho g, \quad (7)$$

where z is the vertical distance from the base of the atmosphere. It is a reasonable approximation for the present purpose to apply the equation of state for an ideal gas,

$$\rho = \frac{Mp}{RT}, \quad (8)$$

where M is the mean atomic weight, T is the temperature and R is the universal gas constant. Therefore, the density and pressure can be expressed in the following form:

$$\rho(z) = \rho_0 \frac{T_0}{T(z)} \exp \left[- \int_0^z \frac{1}{\Lambda(z)} \right], \quad (9)$$

$$p(z) = p_0 \exp \left[- \int_0^z \frac{1}{\Lambda(z)} \right], \quad (10)$$

where ρ_0 and p_0 are the initial density and pressure at the lower boundary of the domain. $\Lambda(z)$ is the pressure scale height defined as

$$\Lambda(z) = \frac{RT(z)}{Mg}. \quad (11)$$

For a gravitationally stratified, nonisothermal atmosphere the cutoff period P_{ac}

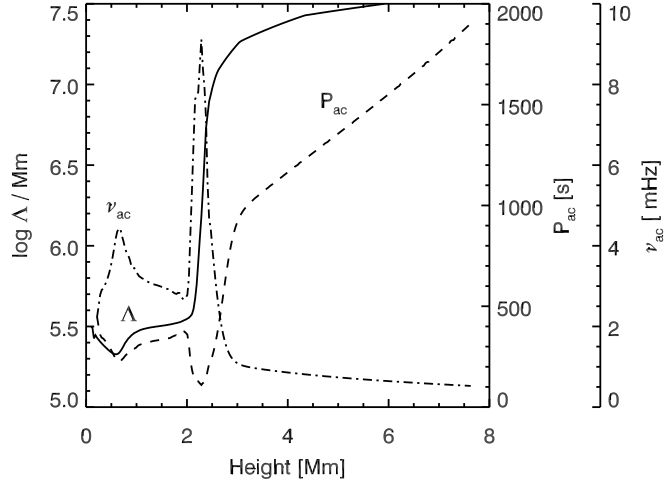


Figure 3. Variation in the pressure scale-height Λ (solid line), the acoustic cutoff period P_{ac} (dashed line) and the cyclic frequency ν_{ac} (dash-dotted line) with changing height as derived from the solar atmosphere model.

is given, for example, by Roberts, 2004 as

$$P_{ac} = \left(\frac{\gamma g}{4\pi C_S} \sqrt{1 + 2\Lambda'} \right)^{-1} \quad (12)$$

where C_S is the sound speed, Λ' is the z derivative of the pressure scale height Eq. (11). Under the conditions representing the solar atmosphere, the logarithm of the variation of the pressure scale-height Λ , the acoustic cutoff period P_{ac} and

the cyclic frequency ν_{ac} are shown in Figure 3. It is evident from the figure that the solar atmosphere in our model is transparent for acoustic oscillations with the cyclic frequencies above 9 mHz, which correspond to the oscillation periods less than ~ 100 s. Oscillations with the period of 5 minutes will therefore be evanescent in the purely hydrodynamic case. However, magnetic field (depending on magnetic field configuration) can increase the cutoff period, thus allowing (magneto)acoustic waves to penetrate the transition region and solar corona. On the cutoff frequency under solar atmospheric conditions see Erdélyi *et al.*, 2007.

Initially and during each simulations, (magneto)acoustic waves are excited by a harmonic driver located just under the height corresponding to the temperature minimum of the solar atmosphere ($z = 400$ km). The V_z component of the perturbation has a Gaussian spatial distribution in the x , y and z directions:

$$V_z = A \sin\left(\frac{2\pi t}{\Delta t}\right) \exp - \left(\left(\frac{x}{\Delta x}\right)^2 + \left(\frac{y}{\Delta y}\right)^2 + \left(\frac{z - z_0}{\Delta z}\right)^2 \right), \quad (13)$$

where the amplitude of the driver signal A and the period Δt are varied for different case studies. Two typical case studies will be discussed here: (i) high frequency harmonic vertical velocity driver with a characteristic period ~ 30 s mimicking granular buffeting where the period is well below the acoustic cutoff in the solar atmosphere; (ii) similar driver but with the period of ~ 300 s mimicking the observed spatially coherent vertical global motions at photospheric level. The boundaries of the domain are open with zero velocity gradients across these boundaries.

3. Hydrodynamic simulations

In this Section we show characteristic examples of atmospheric wave propagation excited by (i) a 30 second periodic driver and (ii) a 5-minute periodic driver in hydrodynamic equilibria.

3.1. 30 second driver

Before investigating the direct propagation (or leakage) of the 5-minute signal that may suffer from evanescence both in the upper photosphere and at the transition region, we consider a typical high-frequency driver with a characteristic period of 30 second. The driver's period is well below the acoustic cut-off period at any point in the model (and in the real solar atmosphere), and therefore it allows us to investigate a simple case of strong wave coupling of the photosphere to corona. In the Sun, the propagation of such high frequency waves into the upper corona would be affected (and perhaps even suppressed) by a number of dissipative effects from radiative to viscous damping, ion-neutral collision, etc., what we should bear in mind to avoid over-interpreting the results. The vertical velocity component is perturbed with the amplitude $A = 200$ m/s. The spatial shape of the driver is a smoothed Gaussian ellipsoid. The half widths of the

Gaussian distribution Eq. (13) are: $\Delta x=0.32$ Mm, $\Delta y=0.32$ Mm, $\Delta z=0.12$ Mm. The structure of the vertical (V_z) and horizontal (V_x) components of velocity generated by the 30 second periodic driver at times $t=112, 216, 244$ and 316 s in the computational domain are shown in Figures 4 and 5 as three-dimensional snapshots. The components are shown as two orthogonal vertical cuts through the 3D computational domain. Colors are used to denote the amplitude of the perturbations. Note that all the following results are presented in the same way. The cuts along the y direction for the horizontal velocity component V_x and Mach number for all 3D figures are slightly shifted in the x direction to avoid showing non-informative cuts at exactly the middle of the numerical domain for velocity component V_x and Mach number, which are equal to zero for the cuts across x direction. In the following figures we show only one horizontal velocity component V_x , since the V_y component can be obtained by 90° rotation of the V_x component due to symmetry of the Gaussian driver, which is described above, around the vertical direction z .

The first stage of the wave propagation, captured at the time $t = 112$ s (approximately three and a half periods after the start of the simulation), is shown in Figures 4a and 5a. The generated acoustic waves propagate isotropically across the chromosphere, with a small increase of their amplitude determined mainly by the density profile in this region of the solar atmosphere. The leakage of acoustic waves through the transition region into the solar corona causes the amplitude of the perturbations to increase rapidly (Figures 4b, c, d and Figures 5b, c, d). This behaviour is the consequence of the very strong (realistic) gravitational and temperature stratification in the vertical direction in the domain (see Figure 2). In the solar corona region the amplitude of the propagating waves slowly decreases with height due to redistribution of the wave energy over the increasing surface of the wave front. In addition, Figures 4 and 5 also clearly show some reflection of high-frequency waves from the transition region. The reflected waves are propagating downwards with the amplitude lower than the waves propagating up from the lower atmosphere region. The intense wave interaction in the chromospheric region has straightforward explanation. At every point where the waves outgoing from the driver and reflected from the transition region interact, the amplitude of the velocities is the result of the vectorial sum of the vector velocities of individual waves. When they are in phase (so that the peaks and troughs are exactly aligned with each other), they combine to strengthen the displacement of either wave acting alone. When they are completely out of phase (so that the peaks of one wave are exactly aligned with the troughs of the other wave), they combine towards to cancel each other out. The interference of the incoming waves and those reflected by the transition region produces a standing wave pattern in the region between about 1000 and 2000 km height in the solar atmosphere. The rich pattern is clearly visible in the lower panels of Figures 4 and 5. This wave interaction is demonstrated in both V_z and V_x velocity components, and is comparable to the observational results by e.g. Fleck & Deubner, 1989 and 2D numerical simulations by Erdélyi *et al.*, 2007.

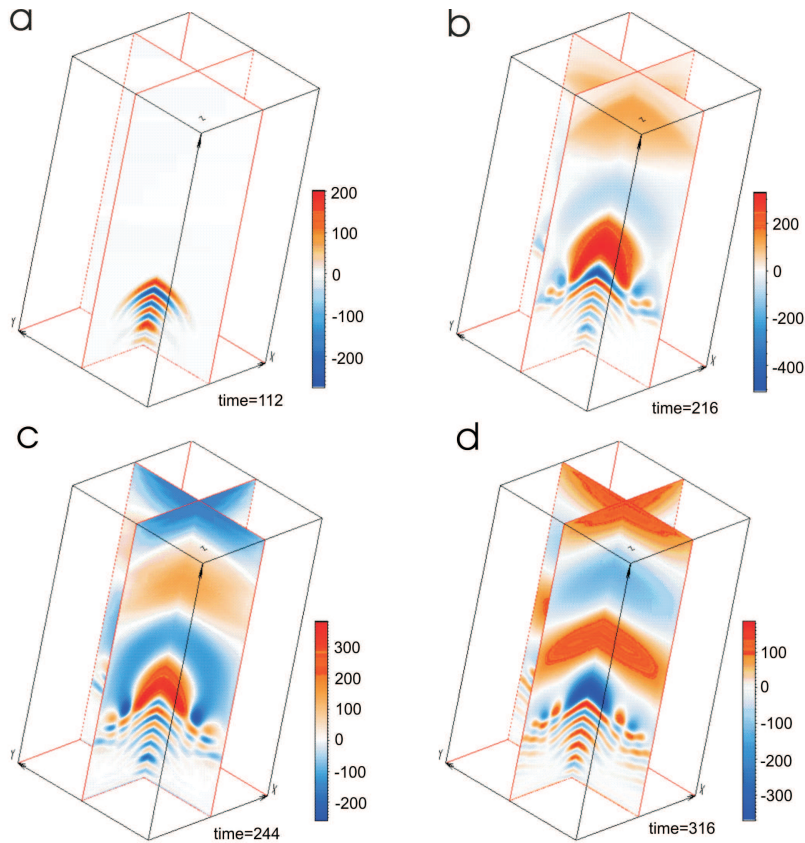


Figure 4. Three-dimensional snapshots of the evolution of V_z showing the development of the initial perturbation in the non-magnetic equilibrium generated by the 30 s periodic driver (in m/s) at the times (a) $t = 112$ s, (b) $t = 216$ s, (c) $t = 244$ s, (d) $t = 316$. The z axis corresponds to height measured in Mm and the x and y horizontal axis are parallel to the solar surface.

3.2. 300 second driver

It is generally accepted that plasma motions at the transition region are often the consequences of the 5-minute p -mode oscillations in the photosphere region (see De Pontieu, Erdélyi and De Wijn, 2003). In this Section, a periodic ($P=300$ s) vertical velocity driver is applied for hydrodynamic equilibria instead of the 30 s driver used in the previous Section.

The medium is now perturbed by an acoustic source with an amplitude $A = 200$ m/s. The driver has been chosen to be characterised with a Gaussian in each spatial direction. The half widths of the corresponding Gaussian, see Eq. (13), are: $\Delta x=0.6$ Mm, $\Delta y=0.6$ Mm, $\Delta z=0.12$ Mm to represent a horizontally spatially coherent perturbation localised in the z direction. The density and the temperature profiles of the solar atmosphere model are similar to those as in the previous Section. The time sequence of the V_z and V_x components of the velocity

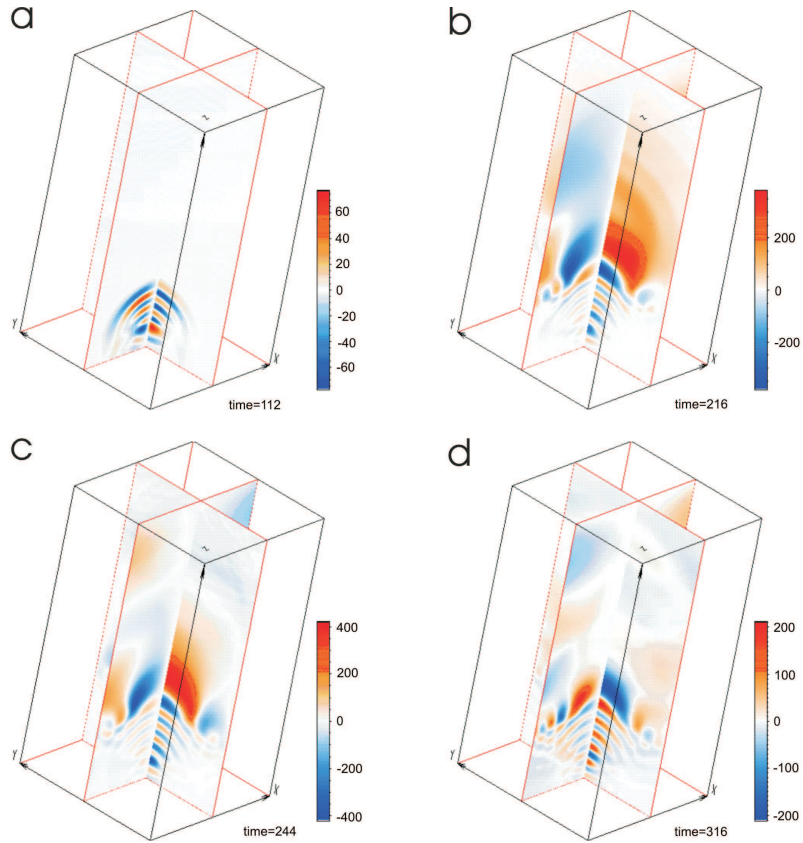


Figure 5. Same as Figure 4 but for the V_x component of the three-dimensional velocity perturbation.

are shown in Figures 6 and 7, respectively. The first transmitted wavefront occurs at ~ 150 s. After a few 5-minute periods two main wave motions are observed in the computational domain. Firstly, there is a clear leakage of the driver signal into the solar corona region. After approximately three periods of the source the amplitude of the vertical perturbation reaches ~ 4000 m/s just above the transition region. Secondly, there is a strong and clearly distinct propagation of waves outwards from the center of the computational domain in the horizontal direction at the transition region (i.e. surface waves). Therefore, the transition region acts, again, as a waveguide for this type of perturbations. The period of these surface waves is around 300 s and the wavelength ≈ 0.8 Mm, dependent on the characteristic spatial extend of the initial driver. Also, it is clear from the figures that a considerable amount of the energy is trapped in the chromospheric cavity.

Comparing these HD simulations with those of Erdélyi *et al.*, 2007 for a 2D atmosphere (i.e. the y -direction was neglected there), we find that there is generally a good agreement in the generation and propagation of the different

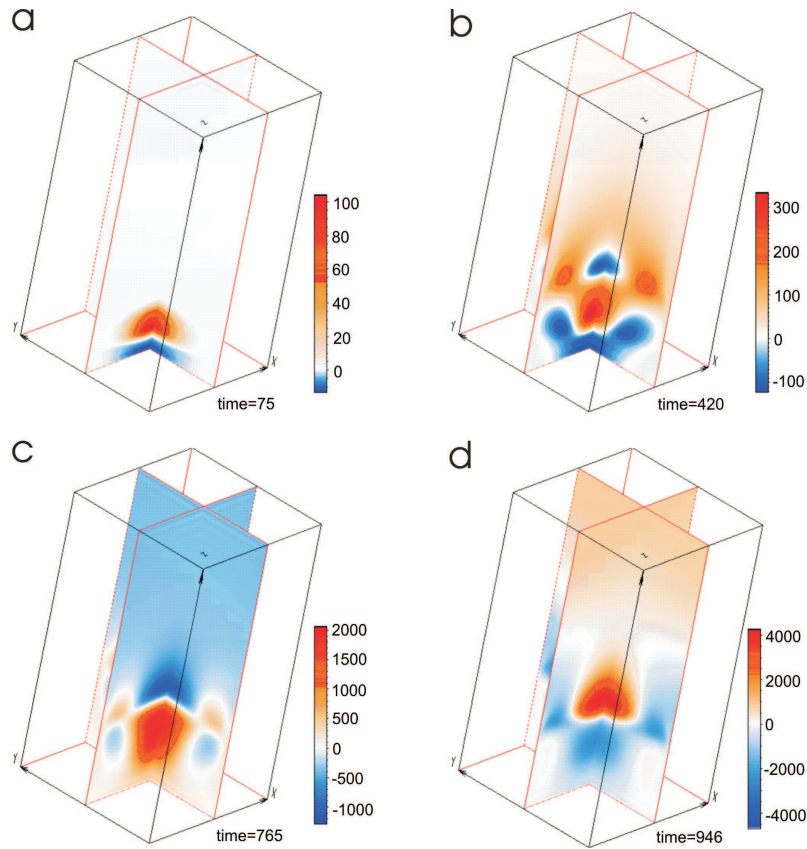


Figure 6. Three-dimensional snapshots of the V_z component of the velocity (in m/s) showing the development of a wave propagation in the non-magnetic equilibrium generated by a 300 s periodic driver at the times: (a) $t = 75$ s, (b) $t = 420$ s, (c) $t = 765$ s, and (d) $t = 946$ s.

wave modes found. Similarly, due to the interference of the forward wave and the wave propagating backwards, the second and the following wave fronts have a decreased amplitude compared to the first wave front. The transition region acts as a guide for the surface waves. Also, the standing wave is observed beyond the lower chromosphere region. These facts assure us that (i) the results found so far are robust, and are not a spurious consequence of 2D geometry; and (ii) the recovery of results of previous 2D simulations are considered as test case for the current full 3D code.

4. Magneto-hydrodynamic simulations

It is now timely and of great interest to study the effect of magnetic field in more realistic 3D solar atmosphere in order to reveal details of the wave propagation there. In this Section, we show results of the numerical solution of the set

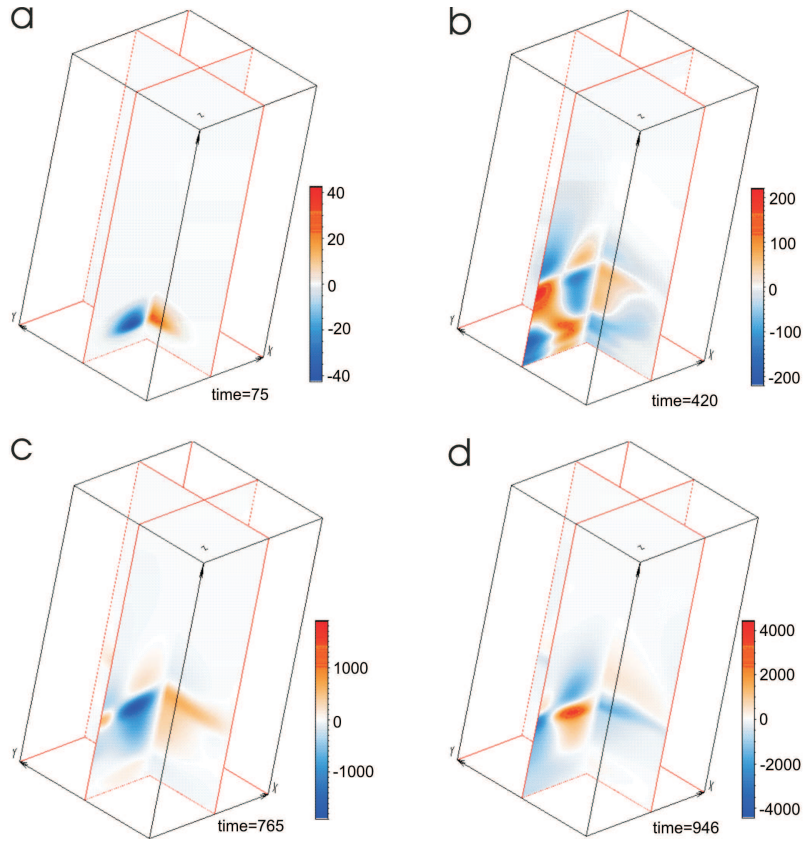


Figure 7. Same as Figure 6 but for the V_x component of the velocity (in m/s) at the times (a) $t = 75$ s, (b) $t = 420$ s, (c) $t = 765$ s, (d) $t = 946$.

of equations (2)-(6) for an environment that is more applicable for the solar atmosphere, where the plasma is embedded in a uniform and straight magnetic field $\vec{B} = (0, 0, B_{0z})$.

Of course, the solar atmosphere has a complex surface magnetic field. Even potential field extrapolations, of the measured magnetic flux at photospheric heights, would result in complex geometric structures outlined by the field lines. However, the uniform field is an excellent tool and a working model to investigate the behaviour of the MHD modes. The magnetic field in our simulations is exactly vertical, which makes the analysis of the wave processes easier, because components of the field perturbations transverse and parallel to the background magnetic field coincide with the horizontal and vertical velocity components in the computational domain. Vertical drivers introduced in our simulations generate both slow and fast types of magnetic wave modes. We address the following questions: which mode can penetrate into the lower corona? How are the modes coupled? How/Can modes transfer energy from the temperature minimum to

the upper chromosphere and the lower corona? And, last but not least, these simulations are useful to test the code in 3D MHD.

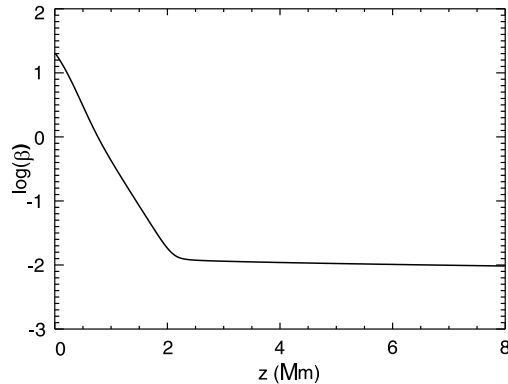


Figure 8. Dependence of the logarithm of plasma β as the function of height z in the modelled solar atmosphere embedded in a uniform magnetic field $B_{0z} = 40\text{G}$

The dependence of $\log(\beta)$ as the function of height z of the equilibrium model at an arbitrary (x, y) point of the computational domain is shown in Figure 8. The plasma β decreases from the value of ~ 20 at the bottom of the simulation domain with height rapidly in the first approximately 2 Mm. The layer with plasma $\beta \sim 1$ is located at the height around 0.8 Mm. Beyond that, from about the top of the transition region, it approaches a nearly constant value of ~ 0.01 . The existence of the layer with $\beta \approx 1$ splits the atmosphere into two different regions: the lower region with the local sound speed greater than Alfvén speed and the upper region with the Alfvén speed greater than the local sound speed.

The region with $\beta \approx 1$ (where it is anticipated that mode conversion region will take place) causes the full or partial conversion of magneto-hydrodynamic waves. In the lower region, where the plasma β is greater than one, slow magnetosonic waves propagate with the local Alfvén speed almost perpendicularly to the magnetic field lines. The properties of this wave are changed after travelling through the mode conversion region. In the region $\beta \ll 1$ the slow wave propagates with the local sound speed parallel to the magnetic field direction. Vice versa, in the lower region, the fast magnetoacoustic wave propagates with the local sound speed isotropically, and in the upper region this wave propagates with the local Alfvén speed perpendicular to the magnetic field. The process of mode conversion has been previously studied for non-realistic models analytically and semi-analytically by e.g. Zhugzhda, 1979, Cally, 2001, McDougall & Hood, 2008, and others.

Note that despite the presented simulations are essentially three-dimensional, we do not observe Alfvén wave motions, since the implemented source is axially symmetric and perturbs only the vertical component of velocity.

4.1. 30 second driver

Following the same approach, as it is presented for non-magnetic simulations described in the previous Section, we introduce the vertical velocity driver with a 30 second period (i.e. high-frequency driver) as a perturbation into the uniform magneto-hydrostatic equilibrium.

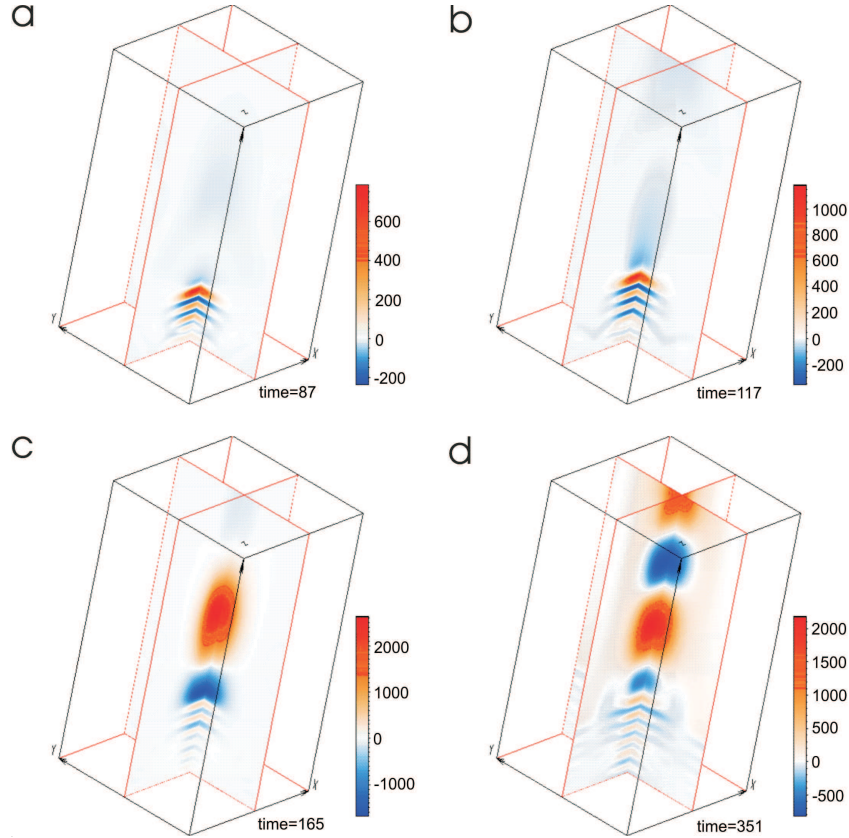


Figure 9. Three-dimensional snapshots of V_z showing the development of the wave pattern in the stratified equilibrium with uniform magnetic field ($B_{0z} = 40$ G). The photospheric driver has a period of 30 s. Snapshot are taken at the times: (a) $t = 87$ s, (b) $t = 117$ s, (c) $t = 165$ s and (d) $t = 351$.

A typical scenario of wave propagation is demonstrated by snapshots in Figures 9 and 10 for the vertical (V_z) and the horizontal (V_x) components of velocity, respectively. In the presence of magnetic field the field lines act as an excellent wave guide. The propagation of the perturbations has a behaviour distinct from that found in the hydrodynamic case. As it has already been shown by Bogdan *et al.*, 2003, the excitation of the slow and fast waves occurs independently from the polarization of the acoustic perturbation source. Thus, the vertically oscillating driver generates both fast (i.e. V_x) and slow (i.e. V_z) magneto-acoustic waves.

Figures 9 and 10 clearly show the difference between the propagation of the high-frequency fast and slow magneto-acoustic waves through the computational domain. The slow waves (see Figure 9), which are mainly localised at the centre of the magnetised equilibrium and propagate parallel to the magnetic field above the mode conversion region, carry the main part of the wave energy to the solar corona. Comparing Figure 4 and Figure 9, it is clear that the amplitude of the slow magnetosonic waves leaking through the transition region for the MHD case is approximately ten times larger than for the acoustic waves generated by the driver with the same amplitude in the HD case. Also, the waves experience a relatively low reflection by the transition region.

From comparison of the wave amplitudes in the vertical direction for the non-magnetic (Figures 4) and magnetic (Figures 9) cases it follows that, in contrast to the non-magnetic case, no significant signature of the standing wave pattern is found in the slow magnetoacoustic mode (V_z) in the simulation (see Figure 9). This is caused by the presence of the magnetic field which leads to the appearance of preferred (vertical) direction in the simulation domain. Therefore, energy tends to propagate along this preferred direction.

The behaviour of the fast magneto-acoustic waves is rather different. Figure 10 provides snapshots for a time sequence $t=87, 165, 234,$ and 351 s of the generated fast magnetosonic wave propagation. The fast magnetosonic waves are observed mainly over the mode conversion layer and under transition region. They tend to propagate in the approximately perpendicular direction to the magnetic field in the region with $\beta \gtrsim 1$ (see Figure 10).

The transition region reflects fast magnetosonic waves and stratification turns them down towards the photosphere region. Thus, the transition region acts as a mirror for the fast waves locked beneath the transition region. The reflected waves interfere with the incoming waves to generate the fine interference structure observable around the driver. This behaviour exactly corresponds to the results obtained by a different method of ray tracing in helioseismology demonstrated by Schunker and Cally, 2006. A less pronounced pattern of standing waves is visible in the fast magnetosonic mode.

4.2. 5-minute driver

Let us now consider the excitation of the waves generated by a harmonic source in the vertical component of velocity with a period of 5 minutes for the case of a uniform and straight weak magnetic field with strength $B_{0z} \approx 40$ Gauss. A harmonic driver is implemented in the same region of the computational domain as in the previous Section. Figure 11 shows a series of illustrative snapshots of the vertical velocity component V_z at the times $t=75, 285, 435,$ and 768 s, respectively. The first snapshot captures the direct propagation of fast/slow magneto-acoustic waves generated by the driver in the lower part of the magnetised solar chromosphere (i.e. where $\beta > 1$, see also Figure 8). The fast wave mode propagates, again, isotropically in the medium until the waves reach the mode conversion region, which is located at the height around 0.8 Mm. The slow mode propagates in approximately perpendicular direction to the magnetic field.

After a penetration and leakage through the transition region (see the latter snapshots) the slow waves transform into non-linear waves in the uppermost

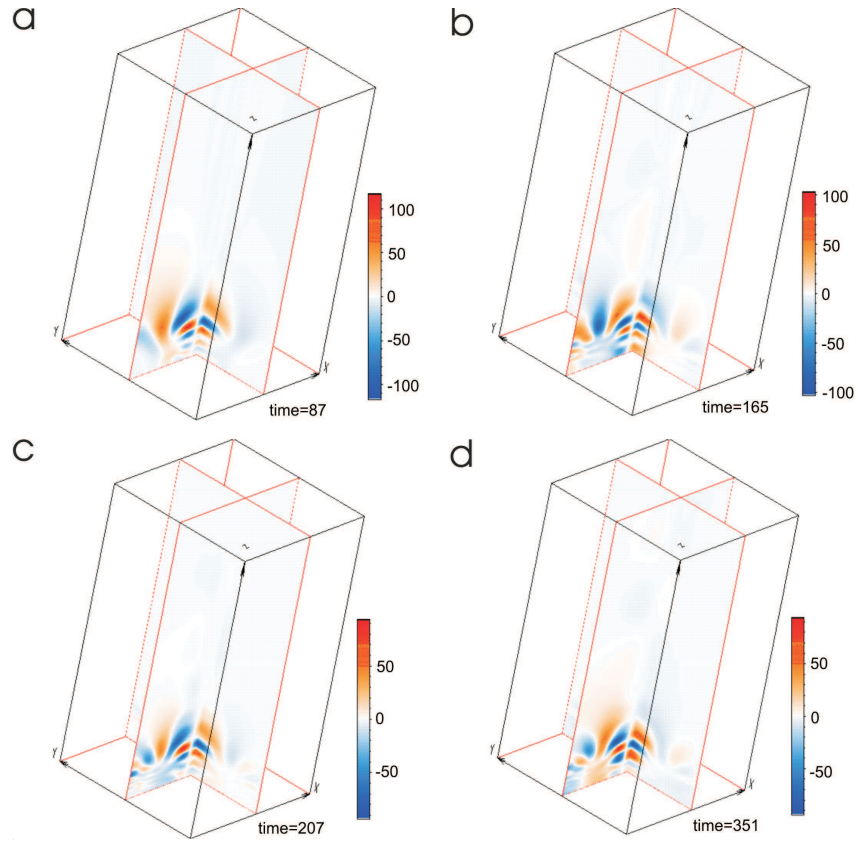


Figure 10. Same as Figure 9 but for the x component of the velocity (i.e. V_x) at the times: (a) $t = 87$ s, (b) $t = 165$ s, (c) $t = 207$ s and (d) $t = 351$.

($\beta \ll 1$) part of the model. The amplitude of the driver is not sufficient for the direct shock wave excitation, but it is enough to change the linear character of the wave propagation towards the coronal region (Bogdan *et al.*, 2003). This transition is caused by the strong decrease of the density and pressure in the transition region (see Figure 2). Compared to non-magnetic simulations (see Figure 6), described in the previous Section, the wavelength of the perturbations propagating along the magnetic field lines increases rapidly with height. This is caused by the increase of the local Alfvén speed towards the top of the simulated solar atmosphere.

Figure 12 mainly represents the temporal evolution of the fast wave component (i.e. V_x) of velocity at the same times as the frames have been shown in the previous figure. Contrary to the simulation with the 30 second driver where almost no energy has been transported by the fast waves, some part (about 20-25%) of the fast mode energy in fact leaks to the solar corona through the transition region. Thus, for the low-frequency driver, energy can be carried to the coronal regions not only by the slow mode, but also by the fast MHD mode.

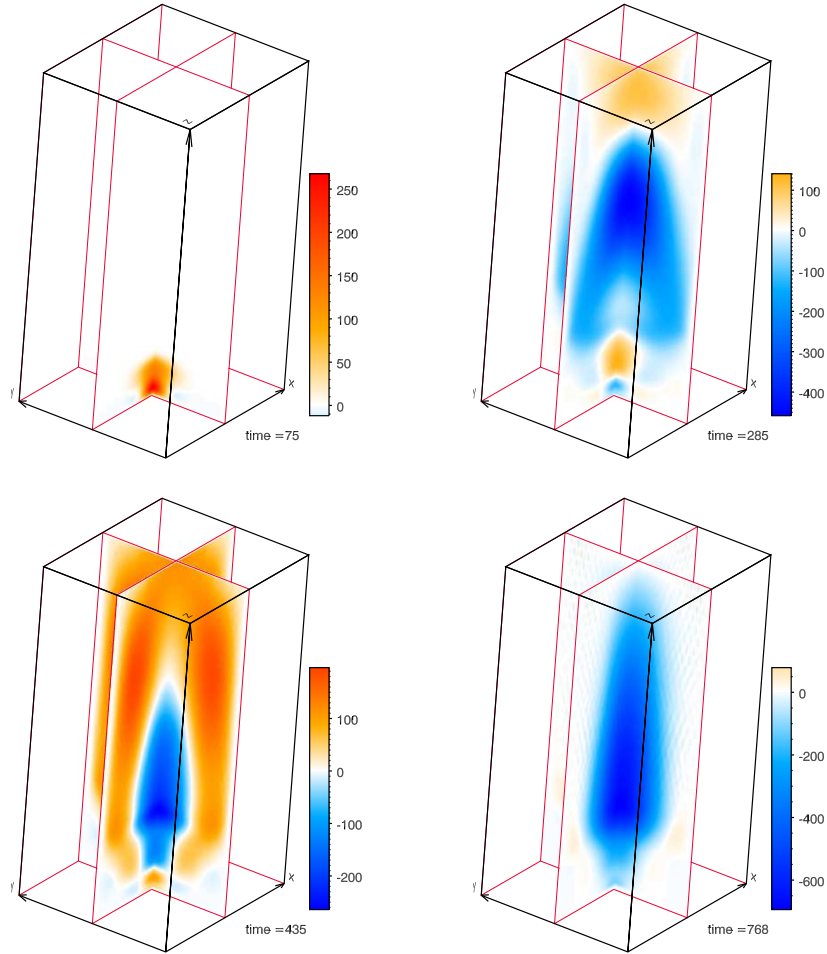


Figure 11. Three-dimensional snapshots of the V_z component of the velocity (in m/s) showing the development of wave propagation at the magnetic equilibrium generated by a 5-minute driver at the times (a) $t = 75$ s, (b) $t = 285$ s, (c) $t = 435$ s, and (d) $t = 768$.

Again, as it was observed in the zero magnetic field case (Figure 6), surface waves are clearly present and visible at the transition region. Surface waves propagate radially in the horizontal direction from the middle of the transition region layer.

There are certain important similarities and distinct differences between the hydrodynamic on MHD simulations. Perturbations propagating in the coronal region of the magnetised atmosphere have the wavelength in the z direction approximately two times larger than in the non-magnetised model. The influence of the magnetic field has a similar broadly spreading character as found in the non-zero magnetic field simulation with the lower period (i.e. 30 second) harmonic driver: the magnetic field lines act as excellent waveguide for the MHD wave leakage and propagating upwards in the domain. Again, the standing wave structure is still visible in a similar way, as it has been shown for the high-frequency simulation. The pattern is observed in the horizontal velocity

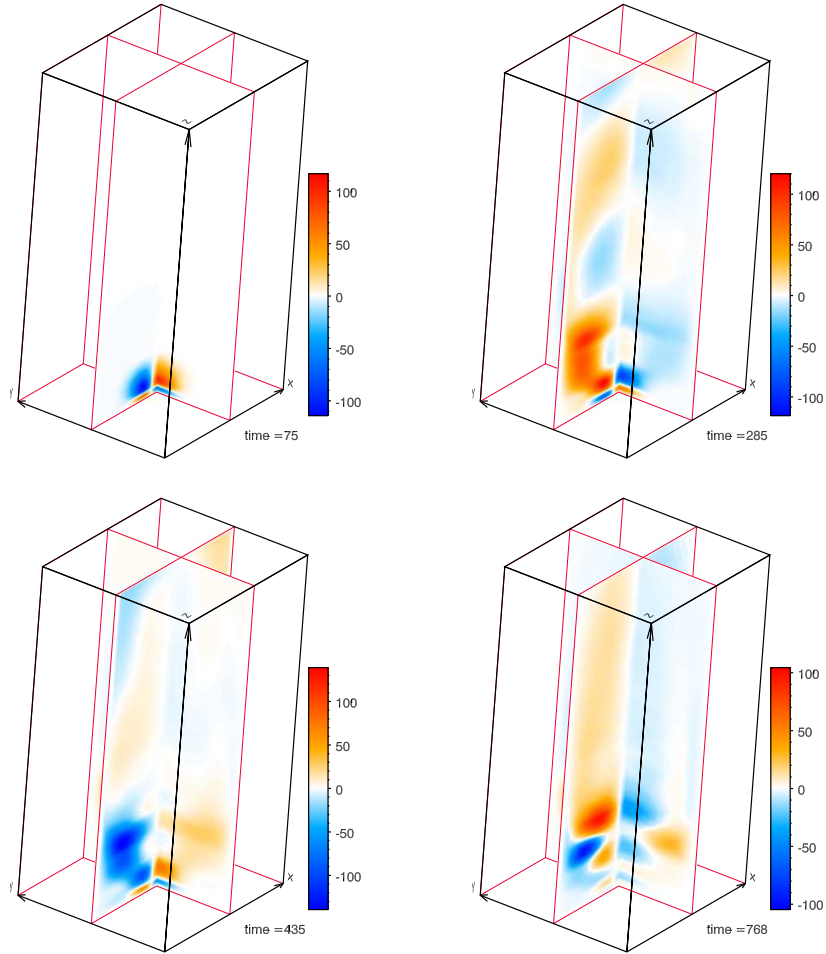


Figure 12. Three-dimensional snapshots of the V_x component of the velocity (in m/s) showing the development of wave propagation at the magnetic equilibrium generated by a 300 s driver at the times: (a) $t = 75$ s, (b) $t = 285$ s, (c) $t = 435$ s, and (d) $t = 768$.

component, characterising mainly the fast mode. However, the vertical velocity component does not show this behaviour. We also found that, the amplitude of the standing wave is significantly lower than in the non-magnetic simulation, because a large part of the wave energy is now transported to the coronal region of the atmosphere by the slow mode.

Figure 13 and Figure 14 show the variation of the Mach numbers, calculated for the velocity components V_z and V_x , which are parallel and perpendicular to the uniform vertical magnetic field, at the times 75, 285, 435, and 768 s respectively. The parallel Mach number increases slightly at the region $\beta \gtrsim 1$ (under the transition region) and rapidly increases in the transition region, as it is evident from Figure 13.

The presence of transition region surface waves is even more pronounced in the Mach number figures than demonstrated by the snapshots of the vertical

and horizontal velocity components. In the transition region the ratio of V_z to the local sound speed reaches the maximum values up to ± 0.065 . In contrast to the forementioned, the horizontal Mach number has approximately the same magnitude and keeps the value of ~ 0.01 in the photospheric and chromospheric regions.

As it is evident from the comparison of these two figures, the vertical Mach number is larger than the horizontal Mach number in the coronal region, and is nearly the same at the photospheric and chromospheric region of the simulation. This consequently means that the main part of the wave energy is transformed to the solar corona by the slow magnetosonic mode, which confirms our previous findings. Also, both slow and fast magnetoacoustic waves are responsible for carrying a part of the energy backwards to the photosphere (Schunker and Cally, 2006), as it has been discussed in the previous Section (see Figures 10 and 12).

5. Conclusions

The 3D MHD model of the solar atmosphere discussed here is a starting point for understanding the different linear and non-linear wave coupling processes in the region spanning throughout from the photosphere up to the solar corona.

In our model we have constructed a strongly stratified background equilibrium which is built on the combination of realistic density and temperature profiles derived from the empirical average quiet Sun model VAL IIIC for the photosphere, chromosphere and transition region and from the McWhirter model for the lower solar corona region.

For the simulations we have run a newly developed code SAC, which is able to solve the full ideal non-linear hydrodynamic and magnetohydrodynamic equations in three dimensions. With SAC, in general, we are capable to investigate a number of processes in magnetised and non-magnetised plasmas under a wide variety of photospheric and solar coronal conditions. The code exploits the hyperdiffusivity and hyperresistivity numerical techniques for stabilisation purposes and uses the variable splitting approach, which makes it possible to keep the domain boundaries transparent for both linear and shock waves.

We have implemented a periodic photospheric wave source with characteristic short and long period perturbations, where the latter corresponds to the frequencies with a power peak observed in the solar atmosphere. From a computational point of view such low frequencies immediately lead to a considerable increase of computational time necessary to cover a required number of source oscillation periods. This makes progress very CPU intensive, challenging and expensive.

A test magnetic field with strength of 40 Gauss is permeated in our model atmosphere. This strength of magnetic field is assumed to represent quiet Sun region. The presence of magnetic field manifests in a significant and physically rich layer right below the transition region, where the plasma β drops just to less than one.

Two sets of simulations were carried out: hydrodynamic and MHD. In both cases two characteristically distinct photospheric drivers were applied: high-frequency ($P = 30$ s) and low-frequency ($P = 300$ s) (magneto)acoustic perturbations; the latter mimicking the power peak in solar global acoustic oscillations.

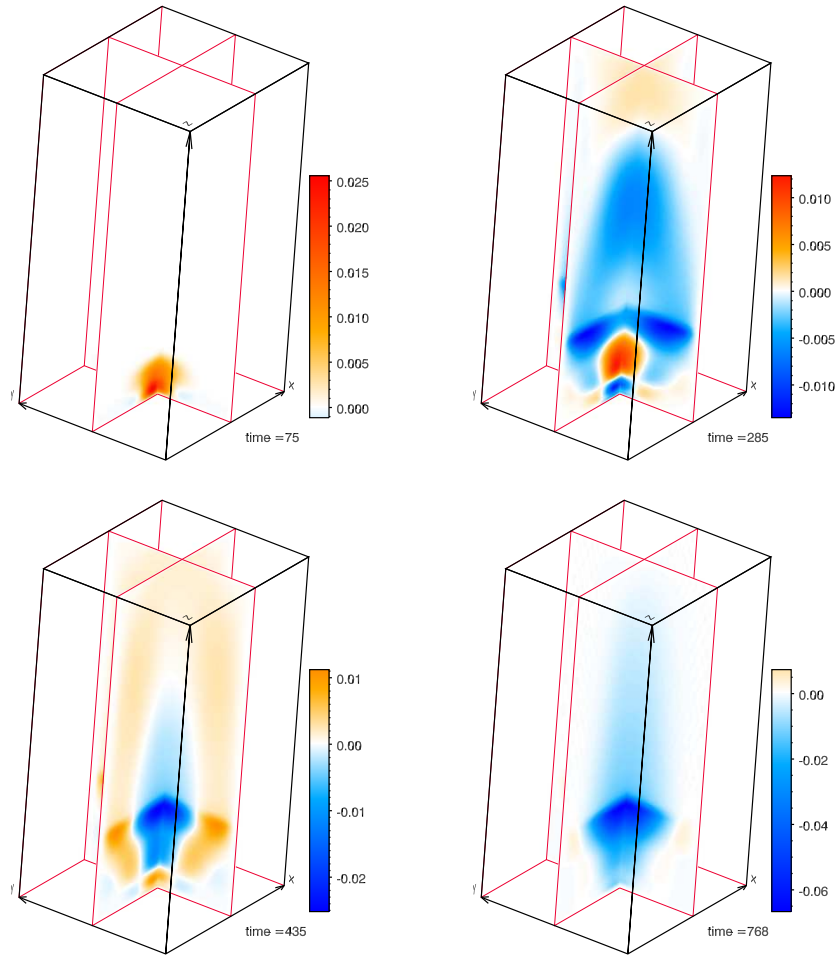


Figure 13. Three-dimensional snapshots of Mach number, calculated for the velocity component V_z parallel to the uniform vertical magnetic background field at the times: (a) $t = 75$ s, (b) $t = 285$ s, (c) $t = 435$ s, and (d) $t = 768$.

Chromospheric standing waves are observed in all four simulation cases that we analysed here. These standing waves are more pronounced in the non-magnetic case. In the MHD computations, a part of the driver's energy is found to be carried upwards by the slow magnetoacoustic mode, thus reducing the amplitude of the fast magnetoacoustic mode, responsible for the formation of standing wave pattern.

We have shown that sufficient amplitudes of a photospheric source can generate fine patterns extending into the non-magnetised and magnetised coronal regions. We found that magnetic field suppresses the energy propagation across the field lines, i.e. the field lines act as an excellent waveguide. It is evident from our numerical modelling, that both low and high frequency signals crossing the transition region are likely to set up transition layer surface waves. Figure 15 depicts the character of the wave propagation in all four cases described above.

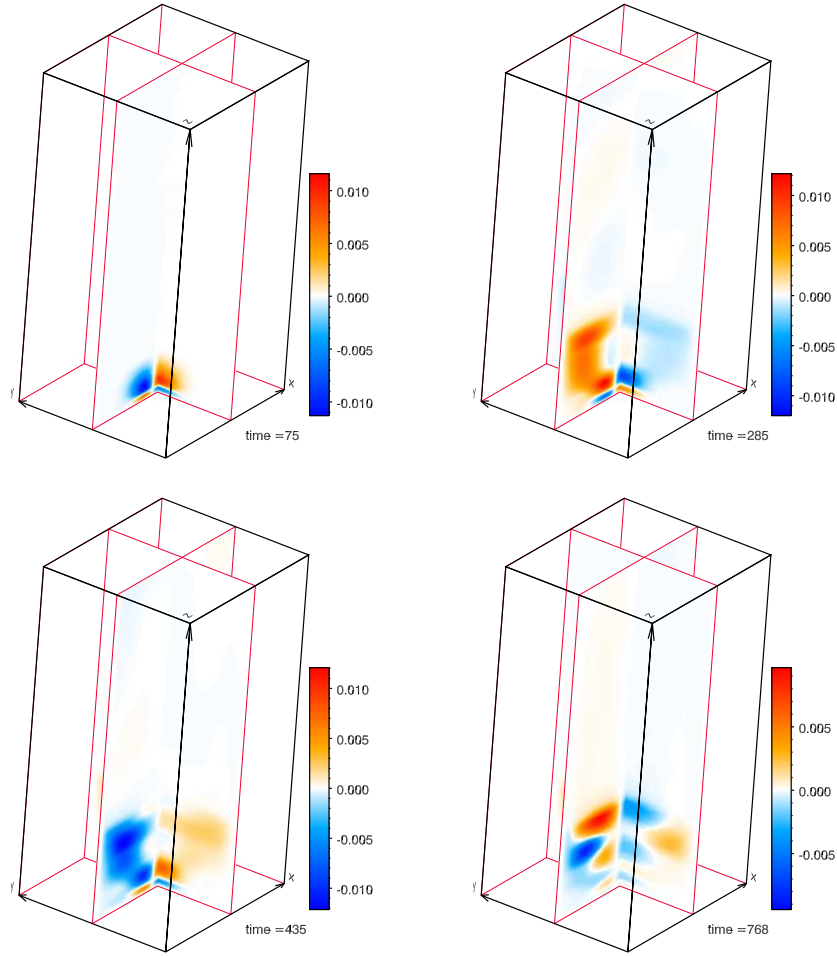


Figure 14. Three-dimensional snapshots of Mach number, calculated for the velocity component V_x perpendicular to the uniform vertical magnetic field at the times: (a) $t = 75$ s, (b) $t = 285$ s, (c) $t = 435$ s, and (d) $t = 768$ s.

The total (thermal + kinetic + magnetic) energy density per unit volume, taken at the central vertical axis of the numerical domain, is shown for the HD high frequency, HD low frequency, MHD high frequency and MHD low frequency simulations in the upper left, upper right, lower left and lower right panels of the figure, respectively. Comparing the 30 s period HD and MHD simulations, it is clear that the waves penetrate into the transition region efficiently due to transparency of the plasma for the waves with the frequencies higher than the cutoff frequency. The amount of the leaked energy in these two simulations is similar. This is not the case for the low frequency models: in the HD simulation, the oscillation amplitude in the middle of the transition region $z \sim 2.5$ Mm (see Figure 2) is about 18 % of the oscillation amplitude as in the same region of the MHD simulation. Also, comparison of the driver amplitude with the amplitude of oscillations at the height $z \sim 4$ Mm (i.e. the solar corona region) shows that

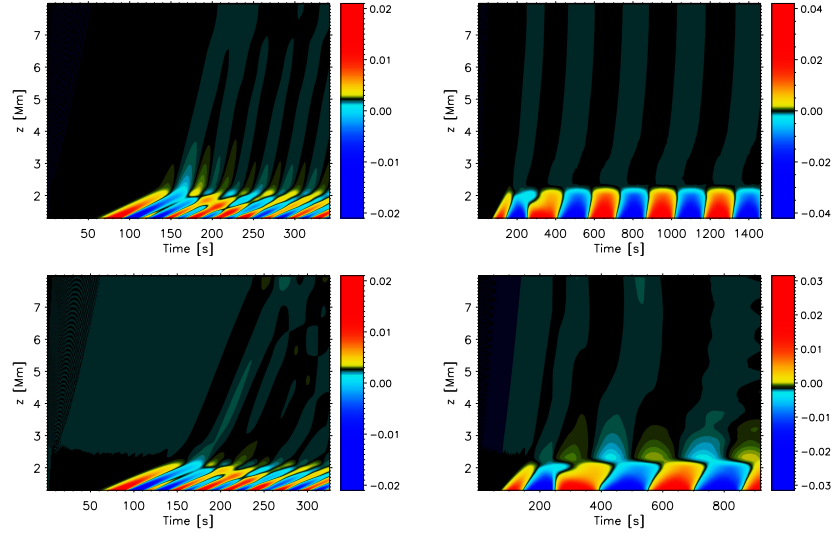


Figure 15. Altitude vs. time images of total energy density per unit volume, measured along the central vertical axis of the computational domain. The four panels of the figure show the HD (upper left panel) and MHD (lower left panel) simulations with a 30 second period harmonic driver and the HD (upper right panel) and MHD (lower right panel) simulations with a 300 second driver. The height below 1 Mm is not shown.

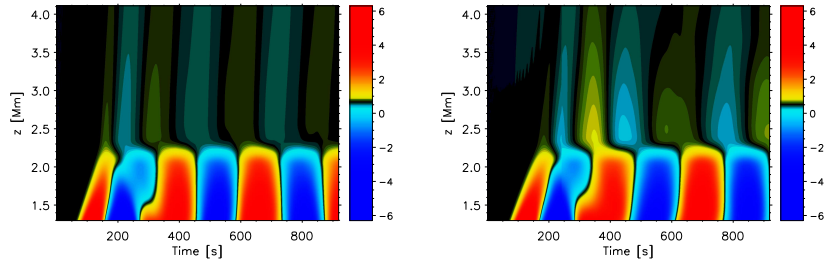


Figure 16. Altitude vs. time images of the total energy density integrated over the horizontal planes. The left and right panels correspond to the non-magnetic and magnetic simulations, respectively. The height range between 1.3 Mm and 4.1 Mm is shown.

in the non-magnetic case the ratio of amplitudes is about 0.05 %, while in the magnetic case the ratio is 0.15 %. However, it is not clear from Figure 15, whether a larger amount of energy leaks to the upper layers of the model in the magnetic case when compared to the non-magnetic one. Figure 16 is to clarify this issue. In this figure, the total energy density integrated over the horizontal planes is shown for 5-minute driver non-magnetic (left panel) and magnetic (right panel) simulations. The range only up to 4.1 Mm is plotted. In this range it is expected that the wave front has not reached the transparent side boundary layers of the numerical domain, so the total energy in the numerical box is conserved. It is evident from comparison of the non-magnetic and magnetic simulations that the amount of total (thermal + kinetic + magnetic) energy transmitted to the corona in the magnetic case is about 2 times larger than in the non-magnetic case

for 5-minute oscillatory driver. Therefore, the larger amplitudes in the magnetic 5-minute oscillation case, shown in lower-right panel of Figure 15, compared to non-magnetic case (see upper-right panel of the same figure) are caused not only by a cumulation of the waves in the preferred direction by the uniform magnetic field, but also by a change in the cutoff frequency, which allows the 5-minute oscillations to penetrate the upper layers of the simulated atmosphere.

We also would like to point out that three-dimensional simulations are rather difficult for visualisation. Sometimes it is not straightforward at all to identify the physical processes in snapshots we have just described. To make the reader more aware of our results, we also provide movies in downloadable electronic form, where the MHD and hydrodynamic wave processes are more clearly identifiable when compared to snapshots.

The movies can be found at <http://robertus.staff.shef.ac.uk/publications/>.

Finally, we would like to comment that Alfvén waves are not excited in the presented 3D numerical simulations due to the nature of the driver implemented. Alfvén waves are of great interest in the context of the MHD wave processes (from energy transfer to energy dissipation by waves) that are essentially three-dimensional. We will consider Alfvénic perturbations in a follow-up study. Future work will also consider the influence of different three-dimensional magnetic field configurations, such as potential or self-similar magnetic fields with the ultimate aim to simulate real magnetic structures derived from observational data, for example from SOHO/MDI measurements.

Acknowledgements The authors acknowledge STFC (UK) for the financial support they received. RE acknowledges M. Kéray for patient encouragement, and is grateful to NSF (Hungary) OTKA K67746. The authors also thank the anonymous referee for suggestions and comments leading to an improved of the paper.

References

- Aschwanden, M.: 2004, *Physics of the Solar Corona. An Introduction*, Praxis, Chichester.
- Banerjee, D., Erdélyi, R., Oliver, R., O'Shea, E.: 2007, Present and Future Observing Trends in Atmospheric Magnetoseismology. *Solar Phys.* **246**, 3.
- Bogdan, T., Carlsson, M., Hansteen, V., McMurry, A., Rosenthal, C., Johnson, M., Petty-Powell, S., Zita, E., Stein, R., McIntosh, S., Nordlund, Å.: 2003, Waves in the Magnetized Solar Atmosphere. II. Waves from Localized Sources in Magnetic Flux Concentrations. *Astrophys. J.* **599**, 626.
- Cally, P.S.: 2001, Note on an Exact Solution for Magnetoatmospheric Waves. *Astrophys. J.* **548**, 473.
- De Moortel, I., Ireland, J., Hood, A., Walsh, R.: 2002, The detection of 3 & 5 min period oscillations in coronal loops. *Astron. Astrophys.* **387**, L13.
- De Pontieu, B., Erdélyi, R., De Moortel, I.: 2005, How to Channel Photospheric Oscillations into the Corona. *Astrophys. J.* **624**, L61.
- De Pontieu, B., Erdélyi, R., De Wijn, A.: 2003, Intensity Oscillations in the Upper Transition Region above Active Region Plage. *Astrophys. J.* **595**, L63.
- De Pontieu, B., Erdélyi, R., James, S.: 2004, Solar chromospheric spicules from the leakage of photospheric oscillations and flows. *Nature* **430**, 536.
- De Pontieu, B., Tarbell, T., Erdélyi, R.: 2003, Correlations on Arcsecond Scales between Chromospheric and Transition Region Emission in Active Regions. *Astrophys. J.* **590**, 502.

- Erdélyi, R., Malins, C., Tóth, G., De Pontieu, B.: 2007, Leakage of photospheric acoustic waves into non-magnetic solar atmosphere. *Astron. Astrophys.* **467**, 1299.
- Fleck, B., Deubner, F.L.: 1989, Dynamics of the solar atmosphere. II - Standing waves in the solar chromosphere. *Astron. Astrophys.* **224**, 245.
- Finsterle, W., Haberreiter, M., Kosovichev, S., Schmutz, W.: 2008, P-mode leakage and Lyman- α intensity. In: Erdélyi, R., Mendoza-Briceño, C.A. (eds.) *Waves and Oscillations in the Solar Atmosphere: Heating and Magneto-Seismology*, Proceedings of the International Astronomical Union, *IAU Symposium*, **247**, 74.
- Gudiksen, B., Nordlund, Å.: 2002, Bulk Heating and Slender Magnetic Loops in the Solar Corona. *Astrophys. J.* **572**, L113.
- Hansteen, V., Carlsson, M., Gudiksen, B.: 2007, 3D Numerical Models of the Chromosphere, Transition Region, and Corona. In: Heinzel, P., Dorotovic, I., Rutten, R.J. (eds.) *The Physics of Chromospheric Plasmas*, ASP Conference Series, **368**, 107.
- Hansteen, V., De Pontieu, B., Rouppe van der Voort, L., van Noort, M., Carlsson, M.: 2006, Dynamic Fibrils Are Driven by Magnetoacoustic Shocks. *Astrophys. J.* **647**, 73.
- Hasan, S., van Ballegoijen, A.: 2008, Dynamics of the Solar Magnetic Network. II. Heating the Magnetized Chromosphere. *Astrophys. J.* **680**, 1542.
- Hasan, S., van Ballegoijen, A., Kalkofen, W., Steiner, O.: 2005, Dynamics of the Solar Magnetic Network: Two-dimensional MHD Simulations. *Astrophys. J.* **631**, 1270.
- Hegglund, L., De Pontieu, B., & Hansteen, V. H.: 2007, Numerical Simulations of Shock Wave-driven Chromospheric Jets. *Astrophys. J.* **666**, 1277.
- Malins, C., Erdélyi, R.: 2007, Direct Propagation of Photospheric Acoustic p Modes into Nonmagnetic Solar Atmosphere. *Solar Phys.* **246**, 41.
- Marsh, M., Walsh, R.: 2006, p-Mode Propagation through the Transition Region into the Solar Corona. I. Observations. *Astrophys. J.* **643**, 540.
- Marsh, M., Walsh, R., De Moortel, I., Ireland, J.: 2003, Joint observations of propagating oscillations with SOHO/CDS and TRACE. *Astron. Astrophys.* **404**, L37.
- McDougall, A.M.D., Hood, A.W.: 2008, MHD mode conversion in a stratified atmosphere. In: Erdélyi, R., Mendoza-Briceño, C.A. (eds.) *Waves and Oscillations in the Solar Atmosphere: Heating and Magneto-Seismology*, Proceedings of the International Astronomical Union, *IAU Symposium*, **247**, 296.
- McWhirter, R., Thonemann, P., Wilson, R.: 1975, The heating of the solar corona. II - A model based on energy balance. *Astron. Astrophys.* **40**, 63.
- Nakagawa, Y.: 1981, Evolution of Magnetic Field and Atmospheric Responses - Part Two - Formulation of Proper Boundary Equations. *Astrophys. J.* **247**, 707.
- Nordlund, Å., Galsgaard, K.: 1995, A 3D MHD Code for Parallel Computers. *Tech. Rep., Astron. Obs. Univ Copenhagen*.
- Oliver, R., Ballester, J.: 1995, Magnetohydrodynamic Waves in a Bounded Inhomogeneous Medium with Prominence-Corona Properties. *Astrophys. J.* **448**, 444.
- Ofman, L., Davila, J.: 1998, Solar wind acceleration by large-amplitude nonlinear waves: Parametric study. *J. Geophys. Res.* **103**, 23667.
- Ofman, L., Nakariakov, V., Sehgal, N.: 2000, Dissipation of Slow Magnetosonic Waves in Coronal Plumes. *Astrophys. J.* **533**, 1071.
- Ofman, L., Thompson, B.: 2002, Interaction of EIT Waves with Coronal Active Regions. *Astrophys. J.* **574**, 440.
- Roberts, B.: 2004, MHD waves in the solar atmosphere. *Waves, Oscillations and Small-Scale Transients Events in the Solar Atmosphere: Joint View from SOHO and TRACE*, Proceedings of SOHO 13, **547**, 1-15.
- Shelyag, S., Fedun, V., Erdélyi, R.: 2008, Magnetohydrodynamic code for gravitationally-stratified media. *Astron. Astrophys.* **486**, 655S.
- Shibata, K.: 1983, Nonlinear MHD wave propagation in the solar chromosphere. I The case of a uniform vertical magnetic field. *Astron. Soc. of Japan, Publications* **35**, 263.
- Schunker, H., Cally, P.S.: 2006, Magnetic field inclination and atmospheric oscillations above solar active regions. *Mon. Not. Roy. Astron. Soc.* **372**, 551.
- Tóth, G.: 1996, A General Code for Modeling MHD Flows on Parallel Computers: Versatile Advection Code. *Astrophys. Lett. and Communications* **34**, 245.
- Vernazza, J., Avrett, E., Loeser, R.: 1981, Structure of the solar chromosphere. III - Models of the EUV brightness components of the quiet-sun. *Astrophys. J. Suppl. Series* **45**, 635.
- Wu, S., Zheng, H., Wang, S., Thompson, B., Plunkett, S., Zhao, X., Dryer, M.: 2001, Three-dimensional numerical simulation of MHD waves observed by the Extreme Ultraviolet Imaging Telescope. *J. Geophys. Res.* **106**, 25089.

Zhugzhda, Y.D.: 1979, Magnetogravity waves in an isothermal conductive atmosphere. *Sov. Astron.* **23**, 42.

